RSC Sustainability

ROYAL SOCIETY OF CHEMISTRY

PAPER

View Article Online
View Journal | View Issue

Cite this: *RSC Sustainability*, 2025, **3**, 546

Utilizing waste lithium-ion batteries for the production of graphite-carbon nanotube composites as oxygen electrocatalysts in zinc–air batteries†

Reio Praats,[a] Jani Sainio,[b] Milla Vikberg,[c] Lassi Klemettinen,[d] Benjamin P. Wilson,[d] Mari Lundström,[d] Ivar Kruusenberg[a] and Kerli Liivand *[a]

The increasing global demand for energy has led to a rise in the usage of lithium-ion batteries (LIBs), which ultimately has resulted in an ever-increasing volume of related end-of-life batteries. Consequently, recycling has become indispensable to salvage the valuable resources contained within these energy storage devices. While various methods have been developed for the recovery of valuable cathode metals from spent LIBs, the anode's active material, graphite, is mostly lost from circulation. This study introduces an innovative method to valorize black mass leach residue, a waste product from industrial hydrometallurgical LIB recycling processes. Predominantly composed of graphite and minor metal residues, this material can be converted into a valuable bifunctional oxygen electrocatalyst. This transformation is achieved by doping the leach residue with nitrogen and through the incorporation of carbon nanotubes into the modified matrix, to enhance the surface area and conductivity of the produced electrocatalyst. These novel catalyst materials can enhance the oxygen reduction reaction and oxygen evolution reaction in zinc–air batteries (ZAB). The best catalyst material exhibited a commendable power density of 97 mW cm^{-2} in ZAB, demonstrating stable performance over 70 hours of continuous charge–discharge cycling. This research represents a significant advancement in the shrewd utilization of LIB recycling waste, which further enhances the goal of closed-loop materials circularity.

Received 29th August 2024
Accepted 16th December 2024

DOI: 10.1039/d4su00526k

rsc.li/rscsus

Sustainability spotlight

This study presents a novel approach to valorizing black mass leach residue, a waste product from lithium-ion battery (LIB) recycling, by converting it into a high-performance bifunctional oxygen electrocatalyst. This research advances global sustainability by recycling end-of-life LIBs into valuable materials, directly supporting SDG 12 (responsible consumption and production) through waste reduction and conservation of critical resources like graphite. By upcycling LIB leach residue into oxygen electrocatalysts for use in zinc–air batteries and fuel cells, the study also promotes SDG 7 (affordable and clean energy). Furthermore, it aligns with SDG 13 (climate action) and SDG 15 (life on land) by reducing waste, fostering green energy technologies, and minimizing environmental impacts associated with resource extraction.

Introduction

As the global production of Li-ion batteries (LIBs) continues to rise, driven by the escalating demand for electric vehicles (EVs), portable electronics, and renewable energy storage solutions, the imperative for efficient end-of-life (EoL) LIB recycling practices has become increasingly pronounced. For example, the demand for LIBs in EVs increased to 550 GW h in 2022, which was equivalent to a year-on-year increase of approximately 65%.[1] Such a rapid rate of increase has raised concerns about the environmental impact related to all aspects of LIBs production, use and EoL management, where incorrect disposal or inefficient treatment methods can be potentially hazardous or lead to a loss of critical resources like Li, Co, Ni, Mn, Al, Cu, and graphite.[2,3] In 2021, the global LIBs recycling capacity estimated to be 180 kT per year, of which 100 kT was based in China.[2] Currently LIB recycling typically comprises of mechanical pre-treatment (discharging, dismantling, crushing, sieving,

---

[a] *National Institute of Chemical Physics and Biophysics, Akadeemia tee 23, 12618 Tallinn, Estonia. E-mail: kerli.liivand@kbfi.ee*

[b] *Department of Applied Physics, School of Science, Aalto University, P. O. Box 15100, 00076 Aalto, Finland*

[c] *Department of Chemistry and Materials Science (CMAT), School of Chemical Engineering, Aalto University, P. O. Box 16100, 00076 Aalto, Finland*

[d] *Department of Chemical and Metallurgical Engineering (CMET), School of Chemical Engineering, Aalto University, P. O. Box 16200, 00076 Aalto, Finland*

† Electronic supplementary information (ESI) available. See DOI: **https://doi.org/10.1039/d4su00526k**

magnetic separation *etc.*) followed by hydrometallurgical and/or pyrometallurgical processes to recover valuable metals from the black mass.[3,4] In many cases, hydrometallurgical treatment of spent LIB (SLIB) waste results in a black mass leach residue, which is mainly comprised of graphite (used as an anode active material), Cu/Al from the current collectors as well as other insoluble materials like binder and separator, and some undissolved cathode active materials.[5] There is about 20 wt% of graphite in LIBs which is often unrecovered and is discarded as waste after the recycling process. Recycling graphite is important for both preserving the environment and conserving resources.[6,7] Both the European Commission and the US government have recently listed natural graphite (NG) as a critical material, recognizing its limited number of mining locations worldwide – with China responsible for about 67% of current global production.[8–10] Synthetic graphite is produced from unsaturated carbons, which are heated to 2500 °C, making this process more CO_2 intensive and generally more expensive than production of NG.[11,12] Therefore, there is an urgent need for the recovery and reuse of graphite from EoL LIBs to help reduce reliance on diminishing primary resources. The global transition towards more sustainable and environmentally responsible energy sources has sparked a growing interest in the development of efficient and eco-friendly energy conversion technologies like fuel cells and metal–air batteries. Within this domain the advancement of oxygen electrocatalysts plays a pivotal role in the development and commercialisation of these electrochemical devices.[13–15] Presently, the most effective catalysts for enhancing the oxygen reduction reaction (ORR) are comprised of platinum (Pt) or Pt-alloys supported on carbon carriers.[16] Similarly, for the oxygen evolution reaction (OER), metallic oxides such as RuO_2 and IrO_2 have demonstrated superior performance.[17] While such catalysts exhibit high efficiency, they encounter challenges related to their stability under harsh conditions, which is compounded by reliance on expensive platinum-group metals (PGMs) that renders them commercially undesirable.[17–19] Consequently, the need for more cost-effective and efficient bifunctional oxygen electrocatalysts has led the scientific community to explore alternative materials and methods for energy conversion and storage. Graphite-based and derived materials—including fullerenes, carbon nanotubes (CNTs), and graphene—have been the subject of intense investigation in recent years due to their potential applications as electrocatalysts or support materials for electrocatalysts. This interest can be attributed to their favourable electrical properties, high specific surface area, and the ability to undergo surface functionalisation.[20] For instance, metal–nitrogen–carbon (M–N–C) materials have emerged as highly promising oxygen electrocatalysts for the substitution of their PGM-based counterparts, due to their unique structural and compositional features.[21,22] It is well known that C–N bonds exhibit good electrocatalytic activity towards ORR and this phenomenon derives from the more electronegative N-atoms, which distorts the associated electron cloud, making the C atoms relatively more positive. As a result of this electrochemical modification, the carbon can act as active O_2 adsorption site that leads to increased carbon disorder and enhanced electrical conductivity.[23,24] Typically, these active electrocatalysts incorporate not only carbon and nitrogen, but also transition metals, such as iron, cobalt, or manganese.[23,25] The active centres for the ORR are primarily carbon-coordinated nitrogen atoms, and the presence of metals serve an important role in the formation of pyridinic nitrogen – which has been found to be one of the most active N-groups.[26] In contrast for OER, transition metals and metal oxides, together with pyridinic-N, are considered the active centres that drive the reaction.[27,28] In addition, for bifunctional ORR/OER electrocatalysts, both types of reaction active sites are desirable, typically involving a combination of carbon–nitrogen and metal/metal oxides deposited within the carbon structure.[22,23] One novel and promising avenue of new raw materials for the synthesis of bifunctional oxygen electrocatalysts lies in the upcycling of graphite from LIBs.[6,29–33] In earlier studies, manually extracted graphite from SLIBs has been utilised as a raw material for the synthesis of different carbon support materials as well as nitrogen and metal doped electrocatalysts.[31–33] Our research has previously demonstrated that industrial black mass leach residue can be used as a valuable precursor material for the synthesis of oxygen electrocatalysts.[6,34] In the current study, we take this premise a step further by investigating the electrocatalytic activity of an oxygen electrocatalyst synthesised through the amalgamation of LIB leach residue (as a source of graphite and metals) with CNTs (that can act as spacers within the graphitic structure). To enhance the activity and durability of these catalyst materials, the introduction of different carbon structures as part of a composite is a viable approach that can be particularly effective when CNTs are used in conjunction with another carbon material.[35] The presence of CNTs not only act as conductive pathways, but also as an electron distributing agent on the surface through interaction with the support materials.[36] This concept is aimed at enhancing the specific surface area, porosity, and conductivity of the catalyst material, thereby improving electron mobility, and ultimately increasing the electrocatalytic activity towards both ORR and OER. The synthesis of oxygen electrocatalysts from leach residue presents a twofold advantage: it addresses the imperative for sustainable materials utilization by contributing to European raw material independency and answers to the demands of the new EU Battery Regulation about recycling a minimum of 65 wt% batteries by 2026, while concurrently advancing the development of efficient energy conversion technologies.[37]

Experimental

Synthesis of the catalyst materials

The initial base material used in this research comprised of residue from an industrially produced battery black mass that had been subject to a hydrometallurgical process to extract the majority of cathode metals. Further details regarding the hydrometallurgical treatment of the black mass can be found elsewhere.[7] The residual waste, known as black mass leach residue, served as the main starting material (*Raw Material*) for this study. This *Raw Material* primarily consists of graphite, with additional metal impurity remnants resulting from the cathode active material and current collectors. For the synthesis of active catalysts, two different carbon materials were used, *Raw Material* and commercially available multi-walled carbon nanotubes (CNTs, >95%, XFM13, XFANO, China), to prepare the final composite materials. Both starting materials underwent a different pre-treatment step prior to their combination. The *Raw Material* went through pyrolysis at 800 °C for 1 hour under an Ar atmosphere (99.999%, Elme Messer Gaas, Estonia) to remove organics. The pyrolyzed *Raw Material* was named as *BR*. The CNTs were treated with a 1 : 1 mixture of 0.5 M H_2SO_4 and 0.5 M HNO_3 for 2 h at 50 °C and thereafter, 3 h at 80 °C. Finally, the CNTs were washed with Milli-Q water until a $pH = 7$ was achieved and then they were dried under vacuum. A mixture of carbon materials (*BR* + CNTs), nitrogen source dicyandiamide (DCDA, Sigma-Aldrich, Germany) and polyvinylpyrrolidone (PVP, Sigma Aldrich, Germany, M_w: 40 000), in a weight ratio of 1 : 20 : 0.1, in 3 ml of ethanol/water (2 : 1) was prepared and this mixture was then ball-milled with 5 mm ZrO_2 balls at 400 rpm for a total of one hour (in two separate 30 min sessions with a 5 min pause in between them). The resultant homogeneous material was then dried, before being pyrolyzed at 800 °C for 2 h under an Ar atmosphere. The ratio between carbon materials (*BR* to CNT) was varied: 25–75 wt%, 50–50 wt%, and 75–25 wt%. The acquired catalysts were named *BR25–CNT75-N*, *BR50–CNT50-N*, and *BR75–CNT25-N*, respectively. A detailed block flow diagram of the modification process is shown in Fig. 1. For comparison, pure *CNT-N* without the *BR* was also prepared and tested.

Physicochemical characterisation

The crystallinity and phase composition of the materials were assessed *via* powder X-ray diffraction analysis (XRD, Malvern Panalytical, UK) using a PANalytical X'Pert3 Powder XRD (Cu Kα radiation, $\lambda = 1.54182$ Å), with step size 0.04 at 45 kV and 40 A. Microstructure images were taken with a MIRA3 scanning electron microscope (SEM, Tescan, Czech Republic) using secondary electrons (SE) at 5 kV acceleration voltage. Elemental mapping was conducted with an UltraDry Silicon Drift energy-dispersive spectrometer (EDS, Thermo Fisher Scientific, USA) at 10 kV acceleration voltage. HRTEM images were obtained with a double aberration-corrected microscope equipped with a 200 kV field-emission gun and X-ray EDS detector (JEOL JEM-2200FS, JEOL Ltd, Japan). Raman measurements were carried out with a Renishaw inVia™ Confocal Raman Microscope (Renishaw, UK). The excitation laser ($\lambda = 532$ nm) was focused on the sample using a 50× objective of a Leica microscope. The scattered rays were collected at 180° and a diffraction grating 2400 gr mm^{-1} was applied to separate the wavelengths for detection with a Charge Coupled Device (CCD) detector. Spectral deconvolution was performed in OriginPro software by applying Voigt function. N_2 adsorption–desorption analysis (Anton Paar Novatouch LX4, Austria) was utilised to ascertain the specific surface area and porosity of samples cooled under liquid nitrogen conditions (77 K). Specific surface area was determined using the Brunauer–Emmett–Teller (BET) theory, whereas the pore size distribution was calculated using the Density Functional Theory (DFT) approach. X-ray photoelectron spectroscopy (XPS) was carried out with a Kratos Axis Ultra spectrometer with monochromated Al Kα-radiation using a pass energy of 40 eV, X-ray power of 150 W and an analysis area of approximately 700 μm × 300 μm. The sp^2 carbon 1s peak at 284.5 eV has been used as a binding energy reference. The elemental composition was determined from peak areas of high-resolution core level spectra after Shirley background subtraction using equipment specific sensitivity factors.

Electrochemical RDE testing

The ORR and OER were studied using rotating disc electrode (RDE) method utilizing a Gamry 1010E potentiostat/galvanostat, which employed a 3-electrode setup. The reference electrode used was Ag/AgCl (3 M KCl), with a graphite rod serving as the counter electrode for ORR and a Pt-wire for OER. A glassy carbon (GC, $S = 0.2$ cm^{-2}) electrode coated with selected catalyst material was used as a working electrode. The RDE setup used an Origalys speed control unit and rotator with rotation rates between 3600 and 400 rpm. The prepared catalyst ink had a catalyst concentration of 2 mg ml^{-1} in ethanol, containing 1 μl $mg_{catalyst}^{-1}$ of 5 wt% Nafion™ solution as an ionomer. Subsequently, 4 × 5 μl of catalyst ink was deposited onto cleaned GC electrodes, resulting in a catalyst loading of 0.2 mg cm^{-2}. For better comparison, both *Raw Material* and *CNT-N* were also subjected to testing; the loading for *CNT-N* was set at 0.1 mg cm^{-2} and all recorded potentials were converted to *vs.* the reversible hydrogen electrode (RHE) using the Nernst equation:

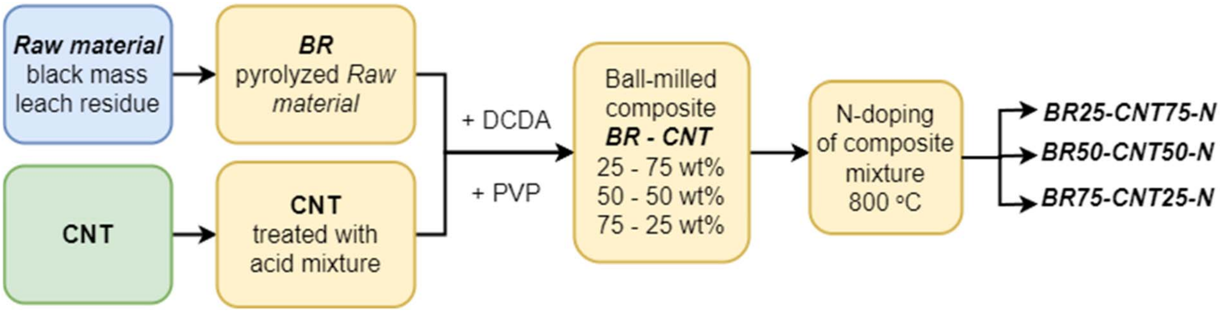

Fig. 1 Block flow diagram of the catalyst preparation.

$$E(\mathrm{RHE}) = E_{\mathrm{Ag/AgCl}} + 0.059\mathrm{pH} + E^{0}_{\mathrm{Ag/AgCl}} \quad (1)$$

where $E_{\mathrm{Ag/AgCl}}$ represents the experimentally measured potential *vs.* Ag/AgCl ($E^{0}_{\mathrm{Ag/AgCl}} = 0.210$ V at 25 °C).

The ORR tests were conducted in an oxygen (Elme Messer Gaas, 5.0) saturated 0.1 M KOH solution at room temperature with a constant O_2 gas flow over the solution and all experiments were controlled *via* Gamry Instruments Framework software. For OER measurements, N_2-saturated (Elme Messer Gaas, 5.0) 1 M KOH solution at room temperature was used, and like ORR, a constant gas flow over the solution was maintained. The *iR*-drop in the OER polarization curves was compensated by adjustment for the systems ohmic resistance that was determined from Electrochemical Impedance Spectroscopy data collected in the frequency range of 100 kHz to 0.01 Hz at the open circuit potential. The resistance was derived from the Nyquist plot by identifying the point where the imaginary part of the impedance reached zero, obtaining the real part as the resistance value. The OER overpotential (mV) was calculated by using ($E_{\mathrm{experimental}}$(*vs.* RHE) − 1.229 V) × 1000. To evaluate the electrocatalytic activity, at least three sets of RDE measurements, each utilizing three electrodes, were performed for each catalyst material synthesized.

Zinc–air battery testing

For zinc–air battery (ZAB) experiments, a custom-made test cell was used. The air electrode, with an active surface area of 1.038 cm^2, comprised a gas diffusion layer (GDL, Sigracet 28BC by SGLCarbon, Germany) and a catalyst layer, with loading of 1 mg cm^{-2}, coated on the GDL. For comparison *CNT-N* material had a final loading of 0.5 mg cm^{-2}, matching the CNT loading used in the studies of the composite material. A Ti mesh served as the air electrode current collector. A commercial catalyst of 20% PtRu (1 : 1 ratio) on carbon support (FuelCellstore, USA) was utilized as an air electrode benchmark catalyst material. The ZAB cell used 6 M KOH + 0.2 M $Zn(Ac)_2$ as an electrolyte and a polished Zn plate (1 mm, 99.9%) as the other electrode. ZAB tests were carried out at room temperature using a PGSTAT30 potentiostat/galvanostat (Metrohm Autolab, The Netherlands) controlled by NOVA 2.1.5 software. Charge–discharge cycling involved alternating 30 minute charge and discharge processes at a current density of 10 mA cm^{-2}. Specific energy density and capacity were determined through complete discharge tests with a current density of 5 mA cm^{-2}, calculated based on the consumed Zn mass. At least three separate ZAB cells were tested for each catalyst material to evaluate the maximum discharge power density.

Results

Physicochemical characterisation of samples

XRD diffractogram (Fig. S1 in ESI† file) of the leach residue (*Raw Material*) prior to pyrolysis revealed a graphite-rich content with various residues from battery components: $Li_{1.44}Co_3O_6$, $LiMn_2O_3$, and CoO – originating from the cathode; Cu and Al_2O_3 – from current collectors and SiO_2 – from additions to anode composition that are used to increase cell energy.[38] A similar combination of elements was also detected by SEM-EDS analysis (Fig. S2†), which additionally revealed the presence of F – resulting from the PVDF binder – and which was subsequently removed during the pyrolysis of the Raw Material. A more detailed description of the Raw Material composition can be found from our previous study.[34] Fig. 2 displays XRD diffractograms of the composite materials prepared from the *BR* and CNTs as well as pure *CNT-N* after the synthesis in comparison with standard cards. All diffractograms exhibited a prominent graphitic carbon peak at 26.5°, with the intensity of this peak diminishing as the CNT content increased, reaching its lowest in the pure *CNT-N* material, where no recycled material was added. This indicates that the graphitic carbon peaks are directly related to the *BR* concentration in the composite. *CNT-N* prepared from the commercial CNTs did not indicate any metal peaks within its diffractogram. The pyrolysis process reduced the metal oxides present in the *Raw Material* and thus *BR* displays the existence of more metallic forms, as evidenced, for example, by the emergence of metallic Co(0) peaks in the final composite materials with no indication of CoO. This transformation suggests the conversion of Co into Co–N–C active centres during the N-doping process.[6,34]

Fig. S3† presents the SEM-SE micrographs of studied materials. *CNT-N* (Fig. S3a†) micrograph shows uniform CNT network. In the case of *BR25–CNT75-N* (Fig. S3b†), an extensive CNT network that includes the presence of some larger particles can be observed. In *BR50–CNT50-N* (Fig. S3c†) and *BR75–CNT25-N* (Fig. S3d†) materials the CNT network is less visible and lighter particles dispersed over the surface are noticeable. SEM-EDS analysis (Fig. S4–S6†) further reveals that a well dispersed mixture of CNT network and *BR* has been achieved in the case of

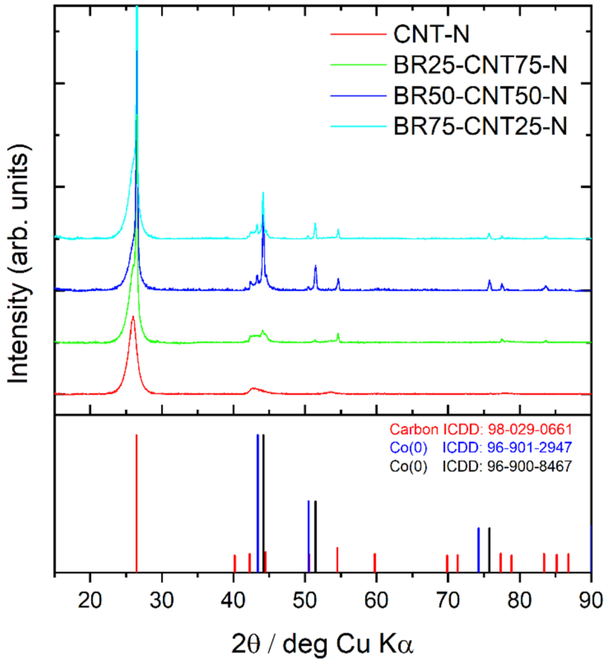

Fig. 2 XRD diffractograms of studied materials with standard cards.

the *BR50–CNT50-N* sample. In *BR75–CNT25-N* sample (Fig. S6†) larger metal agglomerates can be seen from the elemental mapping. From the battery metal residues Co has the highest content in all three composites, however, smaller amounts of Ni, Mn, Al, Cu and Zr were also detected, depending on the *BR* content in the final composite material.

The surface morphology and elemental composition of the prepared catalyst materials were also studied by TEM-EDS as shown in Fig. 3. TEM micrographs show extensive networks of CNTs with some metal and graphite agglomerates. Fig. 3a and S7† show that in the *CNT-N*, the CNT network is evenly distributed. In the case of composite materials (Fig. 3b–d and S8–S10†) some unevenly distributed larger, *ca.* 50–100 nm metal agglomerates as well as sizable graphite particles can be observed. The composite with the highest *BR* content (*BR75–CNT25-N*) had more areas with larger particles when compared to the other composite materials. TEM-EDS of *BR25–CNT75-N* in Fig. S8† shows evenly distributed CNTs with some 10–30 nm particles and several larger 50–100 nm particles also present. These larger particles in Fig. S8† EDS1 and EDS2 have a heterogeneous composition of C, O, Cu, Co, Fe originating from the BR. In contrast, Fig. S9† for *BR50–CNT50-N* shows encapsulated Co particles within the CNTs as well as a larger 50 nm Co and C area. Co particles can act as a catalyst during the nitrogen doping process for the formation of bamboo-structured carbon nanotubes with the Co particles being encapsulated into the nanotube (Fig. S9 location EDS1 and Fig. S10 location EDS1†).[6,39] This demonstrates both the growth of bamboo CNTs as well as the distribution of metal residues and graphite particles. In the case of *BR75–CNT25-N* it was also possible to see bamboo nanotubes and encapsulated Co nanoparticles – as shown in Fig. S10† – but an additional dense population of *BR* metal and carbon fragments were also found to be present. The encapsulation of Co particles can increase the stability of Co particles in harsh environments which is necessary for good electrocatalysts.[40]

For all samples displayed in Fig. S11,† the characteristic Raman modes of multiwalled carbon nanotubes can be distinguished.[41] The three most prominent peaks are the first order G-band at approximately 1580 cm^{-1}, which are characteristic for graphitized sp^2 carbon materials, the defect induced D-band at around 1350 cm^{-1} originating from double resonant Raman process, and its overtone G′-band at approximately 2700 cm^{-1}. Additionally, a shoulder is observed on the G-band at approximately 1620 cm^{-1} associated as D′-band and a broad combination mode D + D′ band at around 2950 cm^{-1}. Both are related

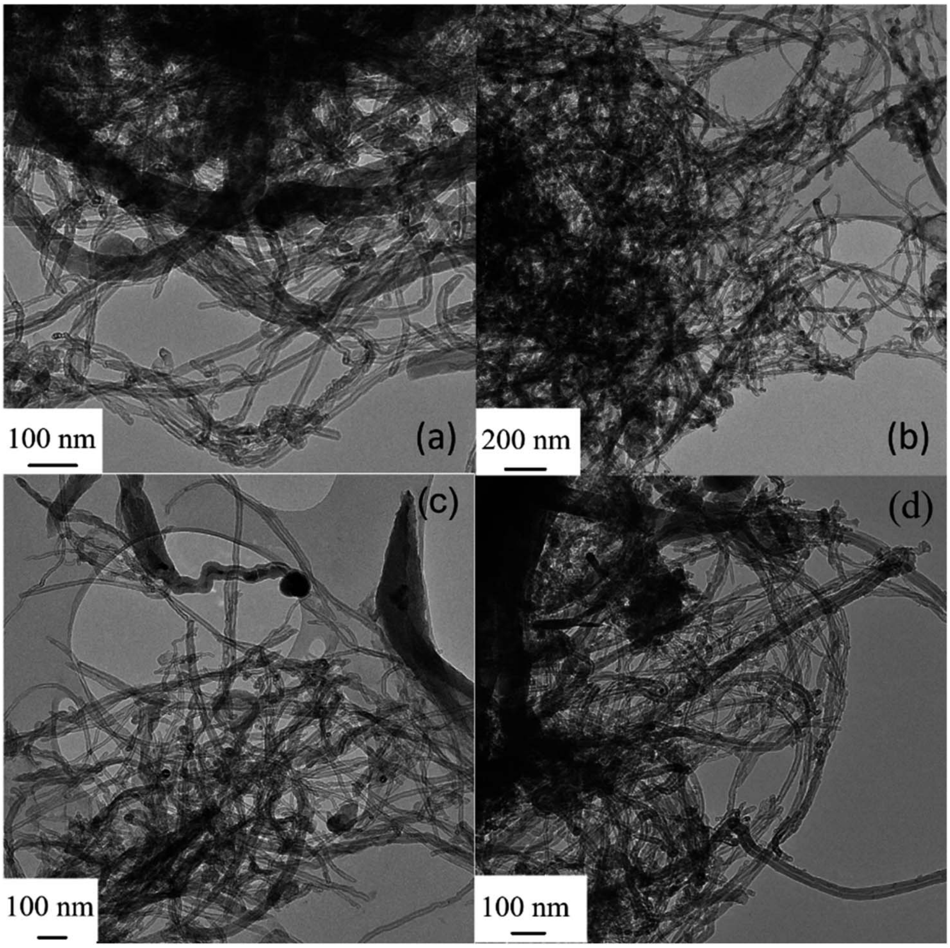

Fig. 3 TEM micrographs of (a) *CNT-N*, (b) *BR25–CNT75-N*, (c) *BR50–CNT50-N*, and (d) *BR75–CNT25-N* catalyst materials.

to defects.[41] Acid treatment generally leads to a higher ratio between the intensities of the D- and G-bands (I_D/I_G).[41] After a heat treatment, some of the graphitic structure is restored as can be observed from the I_D/I_G ratio decreasing from 0.89 for the acid treated CNT to 0.67 for the N-doped *CNT-N*. Doping by nitrogen most likely results in the observed downshift of the G- and D′-bands from 1580 cm^{-1} to 1575 cm^{-1} and from 1620 cm^{-1} to 1615 cm^{-1}, respectively.[42] The I_D/I_G ratio for composite materials show that the degree of graphitization is slightly higher for materials with higher *BR* content as illustrated in Fig. S11,† but further changes in the Raman shifts are not observed for the composites with different *BR* ratios.

The specific surface area (SSA) of the composite catalyst materials exhibited a significant increase when compared to the initial *Raw Material*. Moreover, the SSA demonstrated an upward trend with increasing CNTs concentration within the composites, as indicated in Table 1. Fig. S12a† indicates that the composite catalysts have type IV isotherms with a narrow hysteresis loop indicating the presence of broad mesopores which continue to the macropores.[43] The pore size distribution in Fig. S12b† shows that the materials are mostly mesoporous with the pore sizes varying from 9 to 35 nm. The blending of CNTs into *BR* increases the ability to host more active centres and improves mass transport within the material.

XPS was used to study the chemical composition of the samples. Carbon, oxygen, nitrogen, and various metals (Co, Mn, Ni, Al, and Cu) were detected within the samples (Table 2). Fig. S13a† shows that the C 1s spectrum consists of a main asymmetric peak at 284.5 eV which can be assigned to sp^2 carbon. At binding energies between 285–289 eV there will be some additional contributions from other types of carbon–carbon, carbon–oxygen, and carbon–nitrogen bonding,[44–46] although overall the C 1s spectra show no large variations between samples. Fig. 4 shows the N 1s and Co 2p spectra obtained for the samples. The N 1s spectra in Fig. 4a have been fitted assuming the presence of four types of N-functional groups: pyridinic-N, pyrrolic-N, graphitic-N and N-oxides (for fitting parameters see ref. 47 and 48). The pyridinic-N component will also contain contributions from N–Co bonds but due to the difference in concentrations of N and Co, the pyridinic-N will be more prominent. Based on the fitting, most of the nitrogen is either in pyridinic or pyrrolic form for all samples (Table S1†).

Comparison of the different nitrogen type ratios found within the samples show similar results, except for *BR50–CNT50-N* which has a higher concentration of graphitic-N and N-oxide and less pyrrolic-N. The Co 2p spectra (Fig. 4b) have been fitted with two components: one for metallic Co and one for Co–N which can also contain contributions from cobalt oxides and/or hydroxides.[49–51] Due to the overlap of the Co–N and CoO_x peaks they are represented by only one peak (with fitting parameters for Co(II)[49]). All Co 2p spectra measured can be explained almost solely with this peak. Since no cobalt oxide is observed in XRD for these samples, we attribute this peak to the presence of Co–N. Overall, some clear trends can be determined between the different samples: the amount of nitrogen decreases, and the amount of oxygen increases when going from *CNT-N* to *BR75–CNT25-N*. Additionally, the highest Co content on the composite surface was found to be for *BR50–CNT50-N* sample, following the same trend as shown with SEM-EDS and TEM analysis, higher *BR* content in the composites starts to favour larger agglomerates and limit the dispersion of Co. Uniformly distributed particles increase the active surface area of electrocatalysts.[52]

Table 2 Atomic concentrations (at%) of elements based on XPS data

Sample	C	O	N	Co	Mn	Ni	Al	Cu
N-CNT	88.0	3.2	8.1	0.3	—	—	0.2	—
BR25-CNT75-N	86.5	3.9	7.8	0.5	0.2	0.1	0.6	0.2
BR50-CNT50-N	87.2	5.6	4.7	0.8	0.3	0.1	0.8	0.3
BR75-CNT25-N	88.7	6.2	2.2	0.2	0.3	0.1	1.8	0.3

Electrocatalytic activity towards ORR and OER

The electrocatalytic activity of the prepared catalyst materials were initially tested towards the ORR in O_2 saturated 0.1 M KOH solution (Fig. 5a). For a better comparison, *Raw Material* and *CNT-N* were also tested under same conditions and the electrochemical characteristics are shown in Table 3. The highest onset potential (E_{onset}, j = 0.1 mA cm^{-2}) was demonstrated by the *BR50–CNT50-N* catalyst with a value of 0.914 V *vs.* RHE, followed by *BR25–CNT75-N* and *BR75–CNT25-N* catalyst materials. In comparison, *CNT-N* and *Raw Material* had an E_{onset} of 0.884 V and 0.757 V, respectively, proving the successful modification of the starting materials. The highest half-wave potential ($E_{1/2}$) was also recorded for *BR50–CNT50-N* material at 0.830 V and the limiting current density (j) of the same material was only surpassed by *BR25–CNT75-N* (5.41 mA cm^{-2} *vs.* 5.01 mA cm^{-2}). The presence of Ni, Mn, and Co in the *Raw Material* facilitated the formation of C–N_x and M–N_x moieties and the highest concentration of pyridinic-N was determined for the *BR50–CNT50-N* catalyst, as indicated by increased level of ORR activity.[23]

BR25–CNT75-N and *CNT-N* had similar polarization curve profiles, which comes from the increased surface area and porosity compared to the other composite materials, leading to higher j and $E_{1/2}$ values. Fig. S14a, c, e and g† show the ORR polarization curves measured at different RDE rotation speeds and their related K–L plots (Fig. S14b, d, f and h†). Results

Table 1 SSA of the studied materials

Name of the sample	*Raw material*	*CNT-N*	*BR25–CNT75-N*	*BR50–CNT50-N*	*BR75–CNT25-N*
S_{BET} (m^2 g^{-1})	2.9	63.2	52.9	42.1	27.1

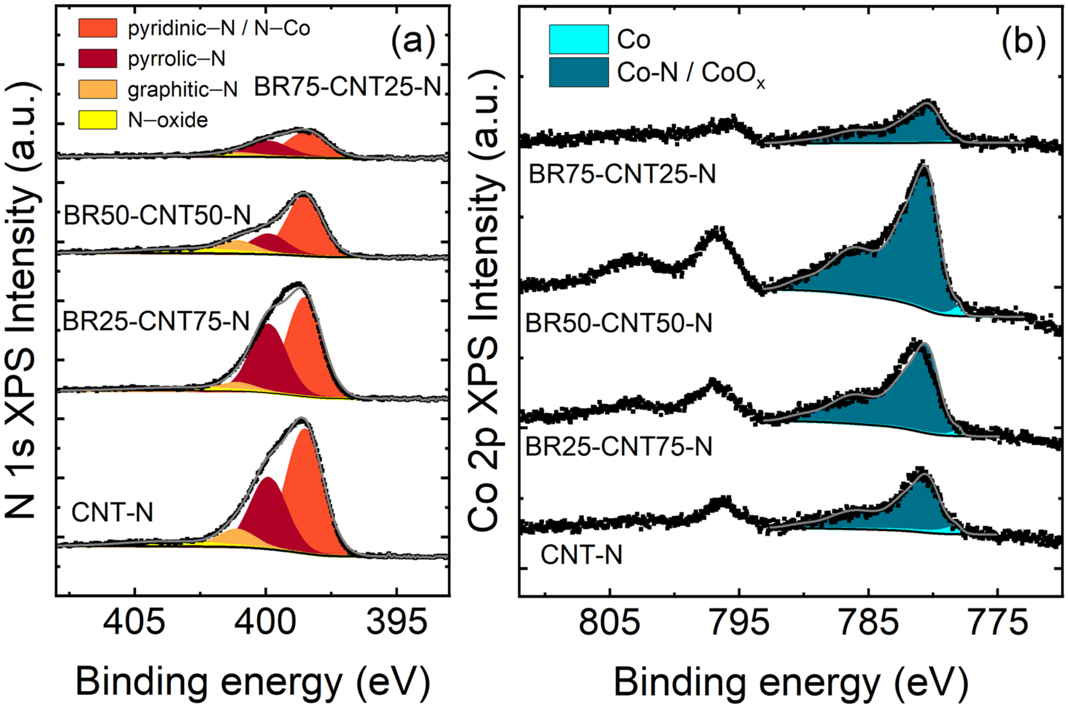

Fig. 4 X-ray photoelectron spectra of the samples: (a) N 1s region and (b) Co 2p region.

demonstrate that all are linear, parallel and have an intercept close to 0 indicating that the process is mass-transfer limited. The *BR50–CNT50-N* catalyst had an *n*-value close to 4 which was stable over the studied potential range – showing a 4e$^-$ pathway for O_2 reduction. In contrast, for *BR25–CNT75-N* the *n* was over 4 and for *CNT-N* and *BR75–CNT25-N* the *n* values were below 4 and gradually decreased at higher potentials, which potentially led to hydrogen peroxide formation *via* 2e$^-$ O_2 reduction. While there remains uncertainty regarding the specific sites that facilitate the 2-electron and/or 4-electron pathways for the ORR, it is suggested that defects within the carbon lattice, particularly those near the ether or carboxylic acid sites, tend to enhance hydrogen peroxide formation.[53,54] Secondly, Co-moieties on the other hand reduce the oxygen molecule directly through the 4e$^-$ pathway to H_2O.[25] Cu and Al, which were also found in the *BR* containing materials, are usually not as active towards the ORR as Co, Fe and Ni.[55,56] In addition, the lower catalytic activity measured for *BR75–CNT25-N* was attributed to the lack of CNTs spacers and insufficient surface area for active centre formation, as well as the higher amount and larger size of metal agglomerates, especially Al. The EIS measurements (Fig. S15a†) were performed on *BR50–CNT50-N*, *N-CNT*, and the *Raw Material* to investigate the influence of CNT addition on the conductivity of the carbon support material. The fitted and calculated charge transfer resistance values indicate that incorporating CNTs enhances the conductivity of the material

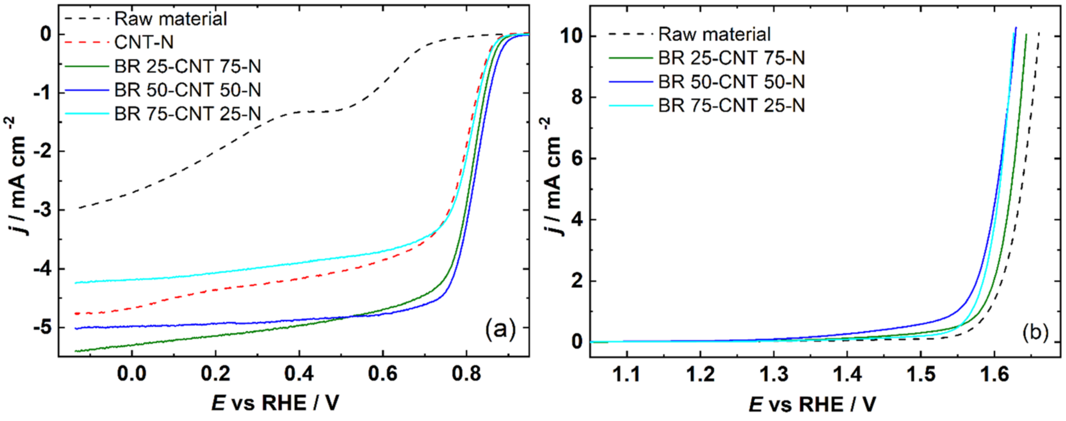

Fig. 5 Comparative (a) ORR polarization curves of studied catalyst materials at 1600 rpm in O_2 saturated 0.1 M KOH solution and (b) OER polarization curves of studied catalyst materials at 1600 rpm in N_2 saturated 1 M KOH solution.

Table 3 Electrochemical characteristics of studied catalyst materials

Catalyst	E_{onset} (V *vs.* RHE)	$E_{1/2}$ (V *vs.* RHE)	j (mA cm^{-2})	OER η (mV)@10 mA cm^{-2}	$\Delta E = E_{\text{OER}}$(@10 mA cm^{-2}) − E_{ORR}(@$E_{1/2}$) (V *vs.* RHE)
Raw material	0.757	0.342	2.96	431	1.318
CNT-N	0.884	0.797	4.76	—	—
BR75-CNT25-N	0.888	0.811	4.23	397	0.815
BR50-CNT50-N	0.914	0.830	5.02	398	0.799
BR25-CNT75-N	0.898	0.816	5.41	414	0.827

compared to the initial *Raw Material*. These findings support the hypothesis that the use of CNTs not only increases the conductivity of the material but also enhances surface area and porosity, enabling the hosting of more active centres and the inclusion of metals from the *BR*.

Fig. 5b shows the OER activity of the same catalyst material. As was the case for ORR, *BR50–CNT50-N* demonstrated the highest activity for OER with E (V)@10 mA cm^{-2} = 1.627 V *vs.* RHE. Similar activity was also found for *BR75–CNT25-N* catalyst material, whilst all others were slightly lower. Such results were to be expected as in OER, the active centres comprise of metal oxides that are more prevalent in the materials with higher *BR* content. Nevertheless, the pure *Raw Material* demonstrated the lowest activity even though it has a high content of metals and metal oxides. However, as these metals/metal oxides are not incorporated within the carbon matrix they can be both easily dissolved within the solution and have a very low surface area when compared to the other catalyst materials examined in this study. Co nanoparticles encapsulated into bamboo nanotubes are protected from corrosion; therefore, materials containing such structures can exhibit higher ORR/OER activity.

For all composite catalyst studied, the ΔE was calculated using formula $\Delta E = E_{\text{OER}}(@10\ \text{mA cm}^{-2}) - E_{\text{ORR}}(@E_{1/2})$ shown in Table 3. Out of all the studied catalysts, the *BR50-CNT50-N* showed the lowest ΔE value at 0.799 V, which shows good bifunctionality of the catalyst materials and even being comparable with some of the best performing catalyst materials shown in literature.[57] Overall, all the N-doped catalysts showed good activity towards the ORR and OER thanks to the synergistic effect of heteronuclear metal doping,[58] especially from the Co nanoparticles encapsulated into bamboo nanotubes.

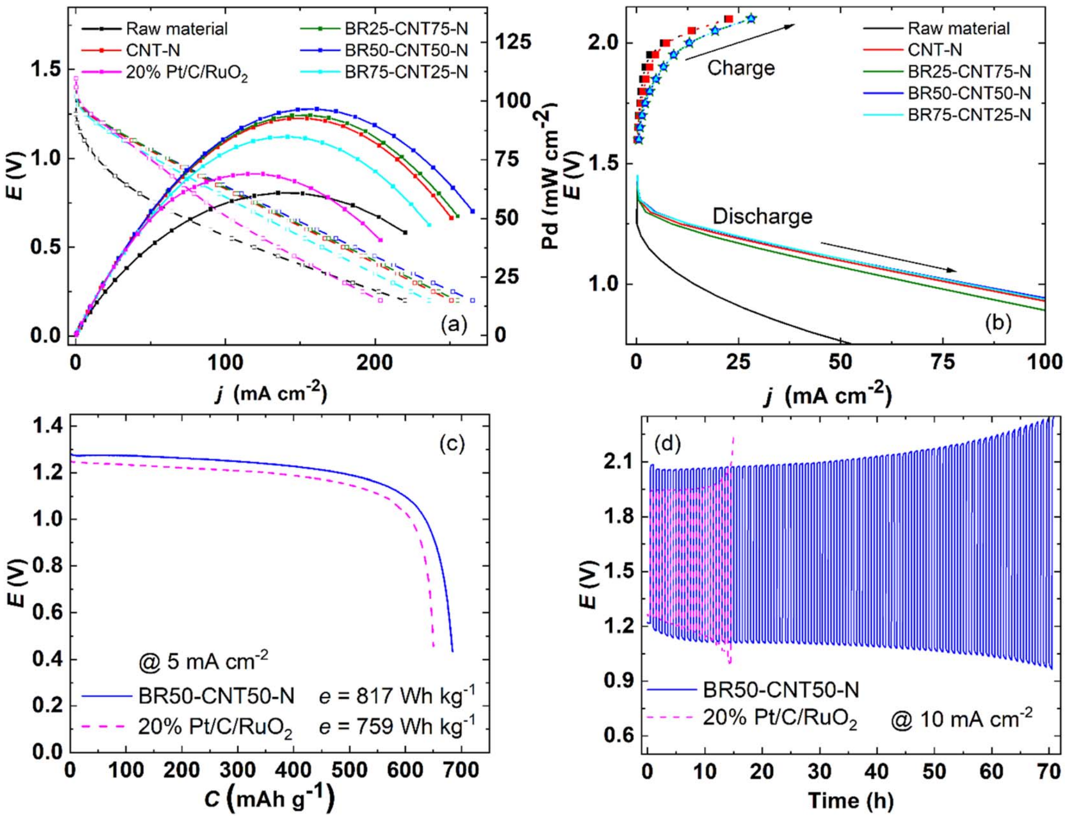

Fig. 6 ZAB results for studied catalysts: (a) discharge polarization curves and power density curves, (b) charge and discharge polarization curves, (c) complete discharge test at 5 mA cm^{-2}, (d) galvanostatic charge/discharge cycling at 10 mA cm^{-2} with 30 min discharge and charge time.

Zinc–air battery air electrode catalyst performance

The prepared catalyst materials were also assessed for their bifunctionality towards oxygen reduction and evolution reaction by incorporation as an air electrode catalyst material in a zinc–air battery. For comparison, a commercial benchmark 20% PtRu/C catalyst was also used as an air electrode catalyst material. All the N-doped catalyst materials examined demonstrated superior discharge powers in comparison to the commercial catalyst (Fig. 6a). The highest power density of 97 mW cm^{-2} at $j = 161$ mA cm^{-2} was shown by *BR50–CNT50-N*, which was expected based on the half-cell test results. Moreover, the maximum power density also exceeded the commercial catalyst's performance by 28 mW cm^{-2} under the same conditions. The power density of all nitrogen-doped materials demonstrated notable performance, highlighting the enhancing capability of nitrogen centres. Additionally, the two composite catalysts (*BR50–CNT50-N* and *BR25–CNT75-N*) exhibited an even higher power density than *CNT-N*, highlighting the synergy between metal and nitrogen active centres. The open circuit potential (OCP) was consistent among all the investigated materials, with only *BR75–CNT25-N* exhibiting a slightly lower value, as illustrated in Fig. S16.† Fig. 6b illustrates the polarization curves for both discharge and charge processes. All examined materials exhibited nearly identical discharge polarization curves, except *Raw Material* which had lower discharge potential. Nevertheless, there was a slight discrepancy in the charge polarization curves, with *CNT-N* and the *Raw Material* displaying marginally higher charge voltages than the composite catalyst. This higher charge potential for the *Raw Material* can be attributed to the presence of non-stable metals in the harsh electrolyte environment, in contrast there are no added metals in the *CNT-N* material, therefore neither of these materials are suitable for the promotion of OER activity.[28] The specific capacity and energy were determined for both the commercial catalyst and *BR50–CNT50-N* catalyst based on data obtained during the complete discharge tests (Fig. 6c). *For BR50–CNT50-N*, the specific capacity and energy were 684 mA h g^{-1} and 817 W h kg^{-1}, respectively. In comparison, the 20% PtRu/C catalyst exhibited specific capacity and energy of 650 mA h g^{-1} and 759 W h kg^{-1}. *BR50–CNT50-N* showed outstanding stability during galvanostatic charge–discharge cycling test for 70 hours, compared to the commercial catalyst, which retained activity for just over 10 hours of continuous cycling as is shown in Fig. 6d. This significant difference in the observed stability and recorded activity between *BR50–CNT50-N* and the 20% PtRu/C catalyst results from the presence of the encapsulated Co particles and Co–N$_x$ active centres within the composite catalyst material.

Conclusions

In this study, a methodology to repurpose lithium-ion battery hydrometallurgical recycling residue as a metal and carbon precursor for the synthesis of active bi-functional oxygen electrocatalysts is outlined. The metal residues in the recycling waste fraction are utilised to achieve *in situ* metal-doping of the catalyst support material. To achieve this, the graphite rich *Raw Material* was combined with carbon nanotubes and nitrogen-doped through ball-milling and pyrolysis processes, to enhance electrocatalytic activity and stability by increasing surface area and through the formation of carbon–nitrogen and metal active centres within the resultant composite materials. Three different ratio combinations of *Raw Material* and CNTs were investigated, with the *BR50–CNT50-N* catalyst material demonstrating the highest electrocatalytic activity.

The notable ORR activity is attributed to the formation of pyridinic nitrogen groups in parallel with a larger surface area, which can host a higher concentration of these active centres. Enhanced activity toward the OER was accomplished by integrating metals into the carbon framework, particularly Co nanoparticles encapsulated within bamboo-like CNTs and through formation of Co–N$_x$ active centres. This improved the activity and, notably, the stability of the catalyst materials, particularly under the harsh alkaline conditions encountered during electrochemical testing. Additionally, the practical applicability of the synthesized catalyst materials was demonstrated by their use as air-electrode catalysts in a rechargeable Zn–air battery. The *BR50–CNT50-N* catalyst exhibited the highest peak power density of 97 mW cm^{-2} and exceptional stability during charge–discharge cycling at a 10 mA cm^{-2} test for approximately 70 hours, significantly outperforming the commercial 20% PtRu/C catalyst. The research work detailed here further exhibits the value of Li-ion battery recycling residue as a resource for the preparation of active M–N–C catalyst materials. By utilizing industrial recycling waste and promoting responsible resource utilization, this approach introduces an innovative and cost-effective method that can repurpose the graphite-rich leach residue fraction from lithium-ion battery recycling process for the development of green energy conversion and storage devices.

Data availability

The data supporting this article has been included as part of the ESI.†

Author contributions

R. P.: conceptualization, investigation, and writing. J. S.: investigation (XPS) and writing. M. V.: investigation (Raman) and writing. L. K.: investigation (SEM-EDS) and writing. B. P. W.: resources and writing. M. L.: resources and writing. I. K.: supervision. K. L.: conceptualization, resources, investigation, supervision, and writing.

Conflicts of interest

There are no conflicts to declare.

Acknowledgements

This research was supported by the Estonian Research Council (PSG926, EAG248), and the Business Finland BatCircle3.0

project (Grant Number 1754/31/2024). In addition, this work was funded by the Ministry of Education and Research through the Centre of Excellence in Circular Economy for Strategic Mineral and Carbon Resources (01.01.2024–31.12.2030, TK228). Use of the facilities provided by Aalto University's OtaNano – Nanomicroscopy Center (Aalto-NMC) and RawMatters Research Infrastructure (RAMI) funded by the Research Council of Finland are also acknowledged as is Hua Jiang for their assistance with the TEM measurements.

References

1 IEA, *Global EV Outlook 2023*, Paris, 2023.
2 IEA, *The Role of Critical Minerals in Clean Energy Transitions*, Paris, 2021.
3 J. Neumann, M. Petranikova, M. Meeus, J. D. Gamarra, R. Younesi, M. Winter and S. Nowak, *Adv. Energy Mater.*, 2022, **12**, 2102917.
4 O. Velázquez-Martínez, J. Valio, A. Santasalo-Aarnio, M. Reuter and R. Serna-Guerrero, *Batteries*, 2019, **5**, 68.
5 A. Chernyaev, B. P. Wilson and M. Lundström, *Sci. Rep.*, 2021, **11**(1), 1–8.
6 K. Liivand, J. Sainio, B. P. Wilson, I. Kruusenberg and M. Lundström, *Appl. Catal., B*, 2023, **332**, 122767.
7 A. Chernyaev, J. Partinen, L. Klemettinen, B. P. Wilson, A. Jokilaakso and M. Lundström, *Hydrometallurgy*, 2021, **203**, 105608.
8 *Study on the Critical Raw Materials for the EU 2023 – Final Report*, Brussels, 2022.
9 U.S. Geological Survey, *2022 Final List of Critical Minerals*, Reston, VA, 2022.
10 *Critical Raw Materials Resielience: Charting a Path towards Greater Security and Sustainability*, Brussels, 2020.
11 J. Asenbauer, T. Eisenmann, M. Kuenzel, A. Kazzazi, Z. Chen and D. Bresser, *Sustain. Energy Fuels*, 2020, **4**, 5387–5416.
12 P. Engels, F. Cerdas, T. Dettmer, C. Frey, J. Hentschel, C. Herrmann, T. Mirfabrikikar and M. Schueler, *J. Cleaner Prod.*, 2022, **336**, 130474.
13 W. Fang, J. Zhao, W. Zhang, P. Chen, Z. Bai and M. Wu, *J. Alloys Compd.*, 2021, **869**, 158918.
14 J. Sun, N. Wang, Z. Qiu, L. Xing and L. Du, *Catalysts*, 2022, **12**, 843.
15 I. Staffell, D. Scamman, A. Velazquez Abad, P. Balcombe, P. E. Dodds, P. Ekins, N. Shah and K. R. Ward, *Energy Environ. Sci.*, 2019, **12**, 463–491.
16 S. Ghosh and R. N. Basu, *Nanoscale*, 2018, **10**, 11241–11280.
17 D. Agrawal, N. Mahajan, S. A. Singh and I. Sreedhar, *Fuel*, 2024, **359**, 130131.
18 X. X. Wang, M. T. Swihart and G. Wu, *Nat. Catal.*, 2019, **2**, 578–589.
19 B. Mohanty, P. Bhanja and B. K. Jena, *Mater. Today Energy*, 2022, **23**, 100902.
20 S. He, M. Wu, S. Li, Z. Jiang, H. Hong, S. G. Cloutier, H. Yang, S. Omanovic, S. Sun and G. Zhang, *Molecules*, 2022, **27**, 8644.
21 H. Chang, S. Cong, L. Wang and C. Wang, *Nanomaterials*, 2022, **12**, 3834.
22 P. Stelmachowski, J. Duch, D. Sebastián, M. J. Lázaro and A. Kotarba, *Materials*, 2021, **14**, 4984.
23 G. Wu, A. Santandreu, W. Kellogg, S. Gupta, O. Ogoke, H. Zhang, H. L. Wang and L. Dai, *Nano Energy*, 2016, **29**, 83–110.
24 J. Duan, S. Chen, M. Jaroniec and S. Z. Qiao, *ACS Catal.*, 2015, **5**, 5207–5234.
25 Y. Zheng, D. S. Yang, J. M. Kweun, C. Li, K. Tan, F. Kong, C. Liang, Y. J. Chabal, Y. Y. Kim, M. Cho, J. S. Yu and K. Cho, *Nano Energy*, 2016, **30**, 443–449.
26 J. Liang and Q. Yuan, *Appl. Surf. Sci.*, 2024, **648**, 159025.
27 J. Heese-Gärtlein, A. Rabe and M. Behrens, *Z. Anorg. Allg. Chem.*, 2021, **647**, 1363–1372.
28 T. Naito, T. Shinagawa, T. Nishimoto and K. Takanabe, *Inorg. Chem. Front.*, 2021, **8**, 2900–2917.
29 L. Alcaraz, C. Díaz-Guerra, J. Calbet, M. L. López and F. A. López, *Materials*, 2022, **15**, 3246.
30 S. Natarajan, M. L. Divya and V. Aravindan, *J. Energy Chem.*, 2022, **71**, 351–369.
31 K. Liivand, M. Kazemi, P. Walke, V. Mikli, M. Uibu, D. D. Macdonald and I. Kruusenberg, *ChemSusChem*, 2021, **14**, 1103–1111.
32 M. Kazemi, K. Liivand, M. Prato, P. Vacek, J. Walmsley, S. Dante, G. Divitini and I. Kruusenberg, *Energy Fuels*, 2023, **38**(1), 659–670.
33 D. Ruan, K. Zou, K. Du, F. Wang, L. Wu, Z. Zhang, X. Wu and G. Hu, *ChemCatChem*, 2021, **13**, 2025–2033.
34 R. Praats, A. Chernyaev, J. Sainio, M. Lundström, I. Kruusenberg and K. Liivand, *Green Chem.*, 2024, **26**, 2874–2883.
35 B. Fang, J. Yang, C. Chen, C. Zhang, D. Chang, H. Xu and C. Gao, *ChemCatChem*, 2017, **9**, 4520–4528.
36 Q. C. Wang, J. Wang, Y. P. Lei, Z. Y. Chen, Y. Song and S. Bin Luo, *Chin. J. Inorg. Chem.*, 2018, **34**, 807–822.
37 *Regulation (EU) 2023/1542 of the European Parliament and of the Council of 12 July 2023 Concerning Batteries and Waste Batteries, Amending Directive 2008/98/EC and Regulation (EU) 2019/1020 and Repealing Directive 2006/66/EC*, 2023.
38 L. Brückner, J. Frank and T. Elwert, *Metals*, 2020, **10**, 1107.
39 X. Wang, S. Jie and Z. Liu, *Mater. Chem. Phys.*, 2019, **232**, 393–399.
40 S. Wang, S. Chen, L. Ma and J. A. Zapien, *Mater. Today Energy*, 2021, **20**, 100659.
41 V. Likodimos, T. A. Steriotis, S. K. Papageorgiou, G. E. Romanos, R. R. N. Marques, R. P. Rocha, J. L. Faria, M. F. R. Pereira, J. L. Figueiredo, A. M. T. Silva and P. Falaras, *Carbon*, 2014, **69**, 311–326.
42 H. Liu, Y. Zhang, R. Li, X. Sun, S. Désilets, H. Abou-Rachid, M. Jaidann and L. S. Lussier, *Carbon*, 2010, **48**, 1498–1507.
43 K. S. W. Sing, D. H. Everett, R. A. W. Haul, L. Moscou, R. A. Pierotti, J. Rouquerol and T. Siemieniewska, *Pure Appl. Chem.*, 1985, **57**, 603–619.
44 T. I. T. Okpalugo, P. Papakonstantinou, H. Murphy, J. McLaughlin and N. M. D. Brown, *Carbon*, 2005, **43**, 153–161.
45 *NIST X-Ray Photoelectron Spectroscopy (XPS) Database Number 20*, Gaithersburg MD, 2000.

46 A. Kousar, I. Pande, L. F. Pascual, E. Peltola, J. Sainio and T. Laurila, *Anal. Chem.*, 2023, **95**, 2983–2991.

47 T. Susi, T. Pichler and P. Ayala, *Beilstein J. Nanotechnol.*, 2015, **6**, 177–192.

48 C. Sheng Chen, J. Bi, Y. Zhao, L. Yang, C. Zhang, Y. Ma, Q. Wu, X. Wang, Z. Hu, S. Chen, J. Y. Bi, Y. Zhao, L. J. Yang, C. Zhang, Q. Wu, X. Z. Wang, Z. Hu and Y. W. Ma, *Adv. Mater.*, 2012, **24**, 5593–5597.

49 M. C. Biesinger, B. P. Payne, A. P. Grosvenor, L. W. M. Lau, A. R. Gerson and R. S. C. Smart, *Appl. Surf. Sci.*, 2011, **257**, 2717–2730.

50 Y. Wang, Y. Nie, W. Ding, S. G. Chen, K. Xiong, X. Q. Qi, Y. Zhang, J. Wang and Z. D. Wei, *Chem. Commun.*, 2015, **51**, 8942–8945.

51 Y. Yao, H. Chen, C. Lian, F. Wei, D. Zhang, G. Wu, B. Chen and S. Wang, *J. Hazard. Mater.*, 2016, **314**, 129–139.

52 Z. Li, H. Sun, L. Wei, W. J. Jiang, M. Wu and J. S. Hu, *ACS Appl. Mater. Interfaces*, 2017, **9**, 5272–5278.

53 Z. Lu, G. Chen, S. Siahrostami, Z. Chen, K. Liu, J. Xie, L. Liao, T. Wu, D. Lin, Y. Liu, T. F. Jaramillo, J. K. Nørskov and Y. Cui, *Nat. Catal.*, 2018, **1**(2), 156–162.

54 H. W. Kim, H. Park, J. S. Roh, J. E. Shin, T. H. Lee, L. Zhang, Y. H. Cho, H. W. Yoon, V. J. Bukas, J. Guo, H. B. Park, T. H. Han and B. D. McCloskey, *Chem. Mater.*, 2019, **31**, 3967–3973.

55 Y. Qin, H. H. Wu, L. A. Zhang, X. Zhou, Y. Bu, W. Zhang, F. Chu, Y. Li, Y. Kong, Q. Zhang, D. Ding, Y. Tao, Y. Li, M. Liu and X. C. Zeng, *ACS Catal.*, 2019, **9**, 610–619.

56 Y. Zhang, Y. Yu, X. Fu, Z. Liu, Y. Liu and S. Li, *Front. Mater. Sci.*, 2020, **14**, 481–487.

57 P. Ganesan, A. Ishihara, A. Staykov and N. Nakashima, *Bull. Chem. Soc. Jpn.*, 2023, **96**, 429–443.

58 J. Feng, C. Ma, Y. Zhang, C. Du, Y. Chen, H. Dong, L. Yu and L. Dong, *Appl. Surf. Sci.*, 2024, **651**, 159219.